

Aerodynamic Shape Optimization of a Dual-Stream Supersonic Plug Nozzle

Christopher M. Heath* and Justin S. Gray*
NASA Glenn Research Center, Cleveland, OH, 44135

Michael A. Park†, Eric J. Nielsen†, and Jan-Renee Carlson†
NASA Langley Research Center, Hampton, VA, 23681

Aerodynamic shape optimization was performed on an isolated axisymmetric plug nozzle sized for a supersonic business jet. The dual-stream concept was tailored to attenuate nearfield pressure disturbances without compromising nozzle performance. Adjoint-based anisotropic mesh refinement was applied to resolve nearfield compression and expansion features in the baseline viscous grid. Deformed versions of the adapted grid were used for subsequent adjoint-driven shape optimization. For design, a nonlinear gradient-based optimizer was coupled to the discrete adjoint formulation of the Reynolds-averaged Navier-Stokes equations. All nozzle surfaces were parameterized using 3rd order B-spline interpolants and perturbed axisymmetrically via free-form deformation. Geometry deformations were performed using 20 design variables shared between the outer cowl, shroud and centerbody nozzle surfaces. Interior volume grid deformation during design was accomplished using linear elastic mesh morphing. The nozzle optimization was performed at a design cruise speed of Mach 1.6, assuming core and bypass pressure ratios of 6.19 and 3.24, respectively. Ambient flight conditions at design were commensurate with 45,000-ft standard day atmosphere.

I. Introduction

Overland noise is a challenge high speed aircraft must overcome to gain regulatory permission to operate in the supersonic regime. Recent conceptual design studies have shown moderate reductions in perceived noise level can be achieved through careful aerodynamic tailoring of the airframe.¹⁻⁴ These studies often neglect powered propulsion, discounting the presence of exhaust jets in nearfield pressure signatures and propagated sonic boom metrics. Furthermore, on-going scale experiments^{5,6} have validated the sonic boom performance of promising low-boom aircraft candidates, but also lack powered nacelles and provide no insight into propulsion-airframe interaction effects. While the amplitudes of discrete pressure disturbances from the propulsion system have been shown minor relative to those induced by the airframe⁷, experimental and computational studies⁸⁻¹⁰ both suggest shock and plume interactions become less negligible for vehicles designed to meet a low-boom standard. In particular, introducing propulsion effects into an optimized airframe boom signature has been found in multiple cases to compromise the low-boom requirement.^{7,10}

To minimize powered propulsion contributions to the overall aircraft boom signature, aerodynamic shape optimization has been applied to an axisymmetric dual-stream supersonic nozzle. The objective of this research is to mitigate nearfield pressure waveforms produced by the isolated nozzle jet without compromising nozzle performance. This successful capability will simplify propulsion-airframe integration for ultra low-boom aircraft and enable propulsion system boom contributions to be further minimized in the presence of an airframe.

While this analysis does not directly consider perceived noise level by a ground observer, the nearfield pressure signature is a known primary driver for sonic-wave propagation theory. Signal attenuation attributed to atmospheric nonlinearities, thermo-viscous absorption and molecular relaxation are acknowledged but considered beyond the scope of this study.

Aerodynamic analysis and design optimization were performed using the computational fluid dynamics (CFD) package FUN3D¹¹. FUN3D is a three-dimensional, node-centered, Euler and Navier-Stokes flow solver for fully

* Aerospace Engineer, Propulsion Systems Analysis Branch, MS 5-10, AIAA Member.

† Research Scientist, Computational AeroSciences Branch, MS 128, AIAA Senior Member.

unstructured grids. Tailored for flow analysis and design, the code offers a discretely consistent adjoint methodology enabling sensitivity calculations necessary for gradient-based mesh adaptation and design optimization.

II. Problem Definition

A. Baseline Geometry

Figure 1 is an isometric view of the baseline geometry, comprised of a centerbody, inner shroud and outer cowl. The geometry was adapted from an axisymmetric expansion plug concept¹⁰ developed by the Gulfstream Aerospace Corporation (GAC) with dual-annular high-flow nacelle bypass exhaust^{12,13}. The original nozzle was created using 1-D gas dynamics and method-of-characteristics (MOC) combined with streamtube shaping, an inverse-design approach for tailoring extensions to the nozzle expansion surfaces to attenuate pressure field disturbances.¹⁰ The core stream passes between the centerbody and inner shroud, while the pressurized high-flow bypass stream, which serves as an aero-acoustic shield, flows between the shroud and outer cowl. During operation, a mechanical actuator linearly translates the centerbody to adjust the effective throat area and maintain performance at off-design. This study only considers nozzle shape optimization of the cruise flight configuration.

The original nozzle reported by GAC contained a centerbody extended significantly longer than that shown in Fig. 1. An extended plug offers the benefits of a reduced momentum wake in the plume and less flow turning near the plug tip. Despite these aerodynamic gains, the added weight penalty and viscous losses along the centerbody surface were reasons a shortened plug variant was created for this study.

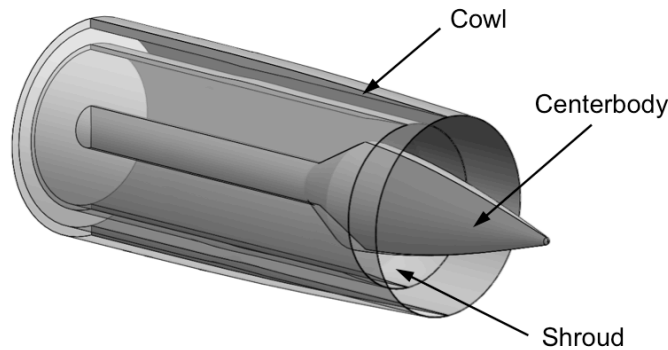


Fig. 1. Isometric view of the baseline plug nozzle.

B. Boundary Conditions

Despite axisymmetric geometry, current limitations of the FUN3D design optimization framework required analysis of a three-dimensional quarter-symmetry sector. The 90-degree computational domain in Fig. 2 was constructed with y - and z -planar symmetry prescribed on the vertical and horizontal surfaces of the domain. The x -axis corresponds to the axial flow direction and is aligned with the nozzle centerline. A farfield Riemann invariant condition was assigned to the outer cylindrical boundary. Subsonic inflow was specified with total temperature and total pressure ratios relative to freestream static conditions for the core and bypass streams. A freestream condition was prescribed on the primary inflow face and a static backpressure permitting supersonic flow that extrapolated from the interior of the domain was applied at the downstream outflow boundary. All nozzle surfaces were modeled as viscous walls with strong enforcement of no-slip.

Bypass and core stream boundary conditions were supplied based on turbine exit conditions provided by GAC. The core nozzle pressure ratio (NPR) or ratio of the total pressure to freestream static pressure was 6.19. The core temperature ratio (NTR) or total core temperature normalized by freestream static temperature was 2.43. The bypass stream NPR was prescribed as 3.24 with corresponding NTR set at 1.51. The freestream reference conditions for cruise corresponded with 45,000-ft standard day atmosphere and a cruise speed of Mach 1.6. The Reynolds number per unit grid length used for solver non-dimensionalization was 7.8×10^6 . Flowfield conditions are summarized in Table 1 where M_∞ , P_∞ and T_∞ represent freestream Mach number, static pressure and temperature, respectively. For reference, the baseline nozzle produces approximately 88,000-N (19,800-lbf) thrust at cruise.

TABLE 1: Flowfield Conditions		
Parameter	Value	Units
M_∞	1.6	-
T_∞	216.65	K
P_∞	14747.89	Pa
Re_{unit}	7.8×10^6	-
NPR_{core}	6.19	-
NTR_{core}	2.43	-
NPR_{bypass}	3.24	-
NTR_{bypass}	1.51	-

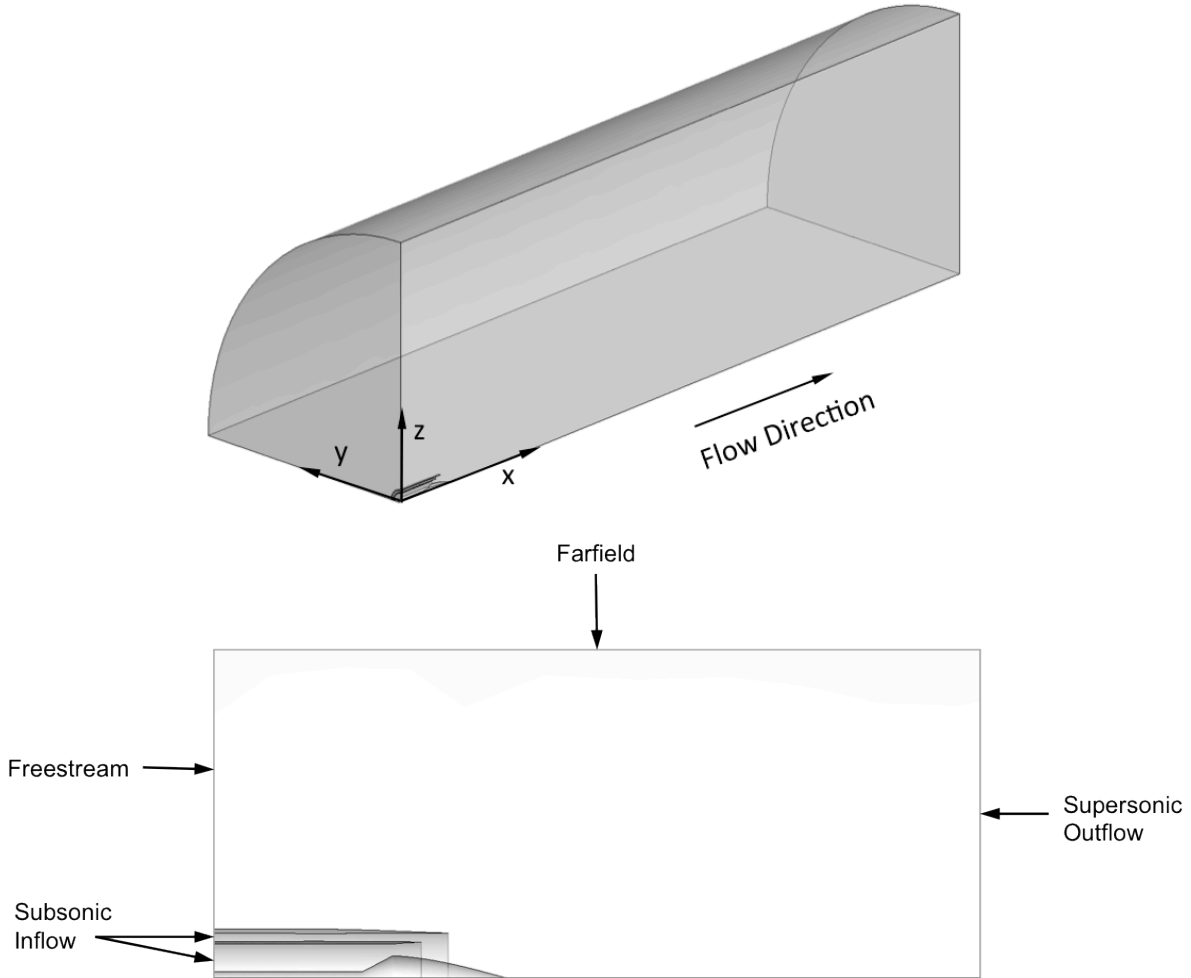


Fig 2. Computational domain and boundary conditions

C. Optimization Problem Formulation

The formal optimization problem may be stated as:

Minimize:

$$f = \sum_{i=1}^N \left(\frac{p}{p_\infty} \Big|_i - \frac{p}{p_\infty} \Big|_i^* \right)^2 \quad (1)$$

Where f is the objective function defined as the sum of squared differences between the local static pressure ratio $\frac{p}{p_\infty}|_i$ obtained along a linear signal at point i and a pre-defined target static pressure ratio $\frac{p}{p_\infty}|_i^*$. For low-boom aircraft shape optimization, a nearfield pressure target is typically specified from a desired low amplitude ground signature based on wave propagation mechanics. The ground signature is defined from an equivalent area target distribution compatible with the vehicle configuration. The characteristic length of the target signature pre-defines the size of the body generating the nearfield pressure disturbance. Unlike vehicle design where aircraft length is pre-determined by mission requirements, the geometric nozzle length is unknown *a priori*. Rather than identify a nearfield pressure target to match using the equivalent area approach, a zero disturbance local pressure field was defined over the entire target distribution. While this target distribution is non-physical, it places no assumed constraints on nozzle length.

The nozzle geometry was constrained in parametric space to maintain core and bypass stream throat areas and avoid compromising nozzle performance during optimization. Thrust was computed using the propulsion performance package in FUN3D that was recently upgraded and verified against the WIND^{14,15} structured flow solver. Thrust was determined by application of the momentum theorem to a control volume about the nozzle. Viscous skin friction and pressure forces were integrated over each solid nozzle surface boundary while axial pressure and momentum fluxes were computed for the core and bypass stream inflow boundaries. Summation of the force and flux contributions combined to give total thrust for the isolated nozzle. If integrated with an airframe, only throttle dependent surfaces would be bookkept with engine thrust. For example, the viscous and pressure forces on the outer cowl surface would be excluded from the engine thrust computation and included as an aircraft drag penalty. Given this study only considers an isolated nozzle, the forces acting on the outer cowl must be included when computing overall nozzle performance.

Axial pressure forces and fluxes within FUN3D were internally normalized by the freestream reference Mach number, pressure and speed of sound as shown in Eq. 2, where F_c is the normalized thrust component for each surface or inflow boundary. The ratio of specific heats is denoted as γ .

$$\text{Thrust} = F_c \left(\frac{\gamma M_\infty^2 p_\infty}{2} \right) \quad (2)$$

III. Geometry Parameterization

To support this work, a new parameterization was developed specifically for axisymmetric geometries and integrated with FUN3D. The implementation used free-form deformation (FFD) with 3rd order B-splines. FFD was selected to parameterize changes to the initial geometry, rather than the geometry directly, resulting in a reduced number of degrees of freedom and simplified design space. The selection of B-splines provided a straightforward means for computing analytic sensitivities.

The FFD approach begins with a B-spline interpolant, defined as a function including parametric coordinate, u , and control point vector, C , of length n , given by Eq. 3. In the definition, $b_{j,p}(u)$ is a polynomial basis function of degree p with knot vector t , and defined recursively by Eq. 4. It should be noted that knot vector selection is non-arbitrary and controls overall spline behavior.¹⁶ Knot spacing was distributed uniformly for each control spline.

$$\text{spline}(u, C) = \sum_{j=0}^n C_j b_{j,p}(u) \quad (3)$$

$$b_{j,p}(u) = \begin{cases} b_{j,0} = \begin{cases} 1 & \text{if } t_j \leq u < t_{j+1} \text{ and } t_j < t_{j+1} \\ 0 & \text{otherwise} \end{cases} \\ b_{j,p} = \frac{u - t_j}{t_{j+p} - t_j} b_{j,p-1}(u) + \frac{t_{j+p+1} - u}{t_{j+p+1} - t_{j+1}} b_{j+1,p-1}(u) \end{cases} \quad (4)$$

The axi-symmetric assumption permits application of 1-dimensional B-splines, which means that u is a scalar, while C is a vector of 2-dimensional coordinates. C is defined here using polar coordinates with r (radial) and x (axial) components. For each individually parameterized nozzle body (centerbody, cowl and shroud), axial locations of the initial and final control points were required to correspond with the axial locations of initial and final points of the discrete baseline geometry.

Once the B-spline interpolant was defined, a mapping was found to link the parametric space of the B-spline with the physical space of the discrete geometry. Each discrete point on the geometry, P_i , was mapped to the B-spline parametric coordinate, u_i , by solving the non-linear system in Eq. 5.

$$\text{spline}(u_i)_x = P_{ix} \quad (5)$$

Given the mapping from P_i to u_i , the total geometric derivatives, $\frac{dP_i}{dC_j}$, were computed using Eqs. 6 and 7. Notably, Eq. 5 is constant with respect to C .

$$\frac{\partial \text{spline}}{\partial C_j} = \sum_{i=0}^n b_{j,p}(u) \quad (6)$$

$$\frac{dP_i}{dC_j} = \left. \frac{\partial P_i}{\partial \text{spline}} \frac{\partial \text{spline}}{\partial C_j} \right|_{u_i} = \sum_{i=0}^n b_{j,p}(u_i) \quad (7)$$

B-spline interpolants were applied in two different ways to individually parameterize the nozzle surfaces. The nozzle centerbody, a closed solid, was deformed using a single B-spline to control radial and axial deformations using Eqs. 8 and 9.

$$\bar{R}_i = R_{i,0} + R_{ref} [\text{spline}(u_i, C_j)] \quad (8)$$

$$\bar{X}_i = \text{spline}(u_i, X_{ref} C_j) \quad (9)$$

$R_{i,0}$ denotes the radial coordinate of the non-deformed geometry at discrete point i . R_{ref} and X_{ref} are parameters used to scale the magnitude of deformations in physical space relative to deformations of the spline. The size of the resulting design space is a function of the number of control points in C . For the centerbody parameterization, each control point contributes two variables (one radial and one axial degrees of freedom) to the design space.

Application of Eq. 7 yields the following derivatives of the deformations in the axial and radial directions with respect to C :

$$\frac{\partial \bar{R}_i}{\partial C_j} = R_{ref} \left. \frac{\partial \text{spline}}{\partial C_j} \right|_{u_i} \quad (10)$$

$$\frac{\partial \bar{X}_i}{\partial C_j} = X_{ref} \left. \frac{\partial \text{spline}}{\partial C_j} \right|_{u_i} \quad (11)$$

The cowl and shroud surfaces, hollow shell bodies, were each divided into inner and outer surfaces and parameterized using a pair of independent B-splines. The first spline was used to control shell centerline profile and was free to move in both radial and axial directions. Each spline centerline control point contributed two variables (one radial and one axial degree of freedom) to the design space. The second spline was used to vary thickness of the geometry about the centerline and was permitted radial motion only. Each thickness spline control point contributed a single variable (thickness degree of freedom) to the design space. Deformations from the centerline and thickness B-splines were combined to define the resultant geometry using Eqs. 12 and 13.

$$\begin{aligned} \bar{R}_{i \text{ outer}} &= \bar{R}_{i,0 \text{ outer}} + R_{ref} [\text{spline}_{center}(u_{i \text{ center}}, C_{center}) + \text{spline}_{thick}(u_{i \text{ thick}}, C_{thick})] \\ \bar{R}_{i \text{ inner}} &= \bar{R}_{i,0 \text{ inner}} + R_{ref} [\text{spline}_{center}(u_{i \text{ center}}, C_{center}) - \text{spline}_{thick}(u_{i \text{ thick}}, C_{thick})] \end{aligned} \quad (12)$$

$$\bar{X}_{i \text{ outer}} = \bar{X}_{i \text{ inner}} = X_{ref} [\text{spline}_{center}(u_{i \text{ center}}, C_{center})] \quad (13)$$

Applying Eq. 7 to Eqs. 12 and 13 yields the derivatives of the radial deformations with respect to each control point, denoted $C_{center \ j}$ or $C_{thick \ j}$.

$$\frac{\partial \bar{R}_{i \text{ inner}}}{\partial C_{center \ j}} = \frac{\partial \bar{R}_{i \text{ outer}}}{\partial C_{center \ j}} = R_{ref} \left. \frac{\partial \text{spline}_{center}}{\partial C_{center \ j}} \right|_{u_{i \text{ center}}} \quad (14)$$

$$\frac{\partial \bar{R}_{i \text{ outer}}}{\partial C_{\text{thick } j}} = R_{\text{ref}} \left. \frac{\partial \text{spline}_{\text{thick}}}{\partial C_{\text{thick } j}} \right|_{\text{ui thick}} \quad (15)$$

$$\frac{\partial \bar{R}_{i \text{ inner}}}{\partial C_{\text{thick } j}} = -R_{\text{ref}} \left. \frac{\partial \text{spline}_{\text{thick}}}{\partial C_{\text{thick } j}} \right|_{\text{ui thick}} \quad (16)$$

It should be noted the derivatives in the axial direction with respect to all thickness control points ($C_{\text{thick } j}$) are zero. The derivatives in the axial direction with respect to centerline control points ($C_{\text{center } j}$) are given by:

$$\frac{\partial \bar{X}_{i \text{ inner}}}{\partial C_{\text{center } j}} = \frac{\partial \bar{X}_{i \text{ outer}}}{\partial C_{\text{center } j}} = X_{\text{ref}} \left. \frac{\partial \text{spline}_{\text{center}}}{\partial C_{\text{center } j}} \right|_{\text{ui center}} \quad (17)$$

At this point, the geometric parameterization has been defined using 2-dimensional polar coordinates. Extension to a 3-dimensional cylindrical coordinate system representative of the actual nozzle geometry was accomplished by keeping the third dimensional angular coordinate, denoted θ , constant during all deformations. Additionally, since the FUN3D deformation mechanics require discrete geometry specification in Cartesian coordinates, the transformations in Eq. 18 were applied.

$$\begin{aligned} Y_i &= R_i \sin(\theta) \\ Z_i &= R_i \cos(\theta) \end{aligned} \quad (18)$$

Similarly, the derivatives were also transformed into Cartesian coordinates. Axial derivatives were unaffected by the change in coordinate system while $\frac{dY_i}{dC_j}$ and $\frac{dZ_i}{dC_j}$ where computed using:

$$\frac{dY_i}{dC_j} = \frac{dY_i}{dR_i} \frac{dR_i}{dC_j} = \sin(\theta_i) \frac{\partial R_i}{\partial C_j} \quad (19)$$

$$\frac{dZ_i}{dC_j} = \frac{dZ_i}{dR_i} \frac{dR_i}{dC_j} = \cos(\theta_i) \frac{\partial R_i}{\partial C_j} \quad (20)$$

In Eqs. 19 and 20, $\frac{\partial R_i}{\partial C_j}$ is the particular partial derivative given in Eqs. 14, 15 and 16 relevant to the specific C_j considered.

The FFD approach using B-splines is demonstrated for the centerbody and cowl geometries in Fig. 3. Each of the deformations shown is completely arbitrary to highlight method flexibility. During the actual optimization, deformations were only permitted downstream of the core and bypass throat areas to satisfy engine mass flow rate requirements during design. Constraining the entrance flow paths for the core and bypass streams also ensured proper geometric integration with the upstream portions of the engine.

The complete geometry envelope for optimization is shown in Fig. 4. All surfaces were further constrained in parameter space to ensure zero or negative thickness regions would not occur. This was accomplished through careful control point placement and selection of conservative variable bounds. For example, localized thinning of the cowl geometry could not result in an intersection of the outer and inner cowl surfaces. Radial deformations of the control point influencing the centerbody tip were also not permitted. In general, the cowl and shroud geometries were restricted from making substantial radial deformations.

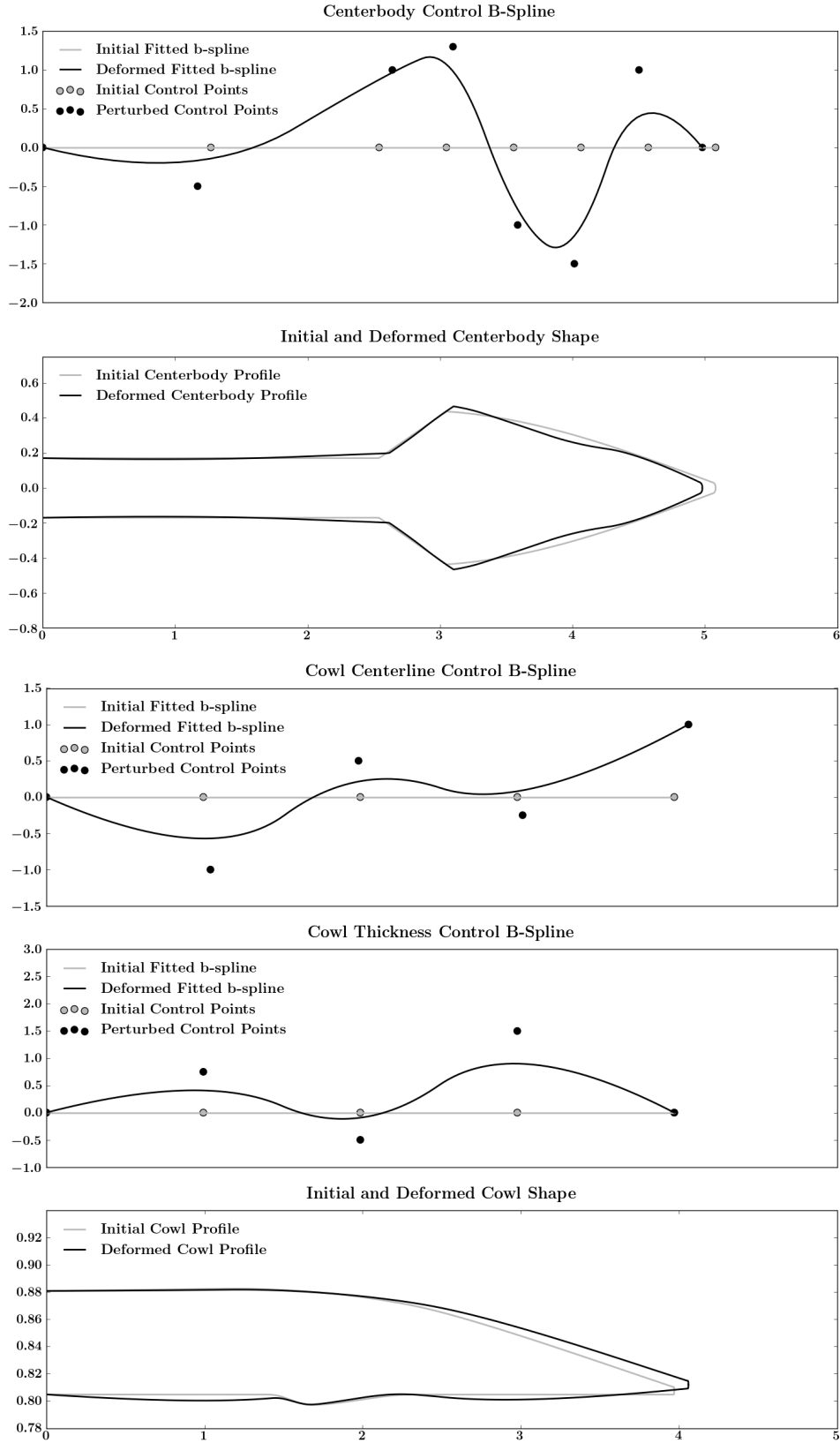


Fig 3. Arbitrary deformations to the centerbody and cowl shapes using B-spline interpolants. Perturbations to uniform B-splines are scaled and mapped back to deform the initial profiles.

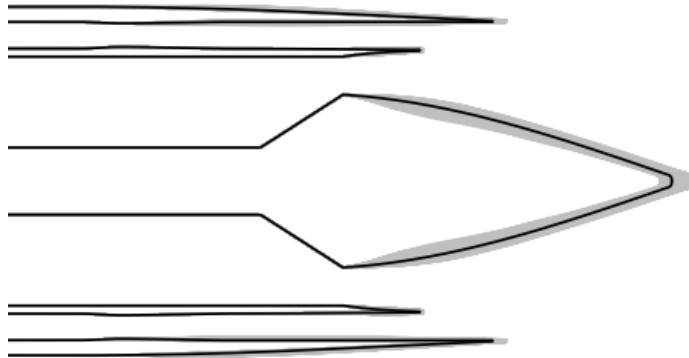


Fig. 4. Baseline nozzle profile (black) can be perturbed via axisymmetric FFD, confined by the physical design envelope (gray).

Example surface sensitivities to the movement of a single cowl centerline control point in the axial direction with respect to the x-axis are plotted in Fig. 5. Discrete analytic sensitivities were computed with respect to Cartesian x-, y-, and z- axes. As expected, the sensitivity appears highest in the vicinity of the control point that was perturbed. All geometric analytic derivatives were verified using finite difference and complex step.

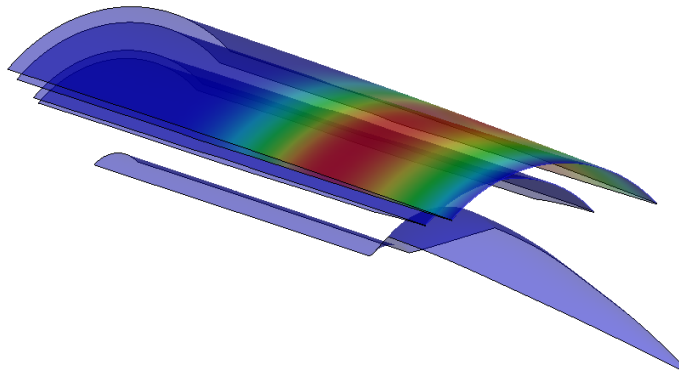


Fig. 5. Cowl surface sensitivities in the x-direction with respect to a single cowl centerline control point axial perturbation.

IV. Flow and Adjoint Solvers

The Fully Unstructured Navier-Stokes Three-Dimensional (FUN3D)¹¹ flow solver is the node-based CFD code applied in this study. FUN3D uses the finite volume method on unstructured grids to solve the discrete Euler and Reynolds-average Navier-Stokes (RANS) equations for compressible and incompressible flows. The solver employs a second-order accurate implicit point-iterative method with CFL scheduling available for convergence acceleration. Fluxes at cell interfaces were computed using the upwind inviscid scheme of Roe¹⁷. The Spalart-Allmaras¹⁸ model was coupled to the mean flow equations for turbulence closure. Domain decomposition was applied to exploit high-performance parallel computing.

Following convergence of the steady-state RANS equations, the set of discrete adjoint equations¹⁹⁻²¹ were solved using a dual-consistent time-marching method.^{22,23} One advantage of an adjoint approach is that sensitivity information can be obtained for an objective function with respect to many design variables at a computational cost comparable to that of a single flow solution. Rigorous sensitivity information from an adjoint solution may also be exploited to guide mesh adaptation and arrive at an, often non-intuitive, grid-converged result. This enables output-based engineering metrics to be captured to a high degree of precision by minimizing associated spatial discretization errors.

During design optimization, volume mesh deformations were accomplished by solution of an analogous linear elasticity problem.^{19,24} Elements near solid wall boundaries were stiffened to conform to prescribed surface

deflections where Young's modulus was inversely proportional to the distance from the nearest solid boundary and Poisson's ratio was assigned a uniform value of zero. All interior volume grid displacements were computed from the finite volume formulation of the elasticity equations using the Generalized Minimum Residual (GMRES)²⁵ algorithm.

All flow and adjoint computations were performed using 600 Intel Haswell processors operating at 2.5 GHz on the NASA Pleiades supercomputer. Each flow or adjoint solution required approximately 1 hour of wall clock time to reach convergence.

V. Optimization Algorithm

Given the high computational cost of RANS CFD, a local gradient-based optimization approach was selected for efficiency. While gradient-free methods like genetic algorithms have higher probability of identifying a true global optimum in the presence of local minima, they require significantly more function evaluations and exhibit slow convergence rates detrimental for aerodynamic shape optimization.²⁶

For the unconstrained optimization performed here, the standalone Sparse, Nonlinear Optimizer (SNOPT)²⁷ was implemented. SNOPT is a gradient optimizer that uses the Sequential Quadratic Programming (SQP) method. A Quadratic Programming (QP) subproblem is solved during each major iteration to determine the next search direction. The SQP algorithm implements a smooth augmented Lagrangian merit function with explicit provision for infeasibility in the original problem and QP subproblems.²⁷ The Hessian of the Lagrangian is estimated using the limited memory quasi-Newton method. SNOPT has been demonstrated proficient for solving large-scale optimization problems containing up to thousands of design variables and constraints.

VI. Adjoint-Based Mesh Adaptation

The baseline tetrahedral 3-D volume grid consisting of anisotropic extruded cells near all nozzle surface boundaries was created using the software Pointwise®. All boundary cells were resolved to a $y^+ < 1$ with the initial volume containing approximately 3.5 million nodes. The z-symmetry plane grid topology and Mach number solution contour are shown in Figs. 6 and 7. The initial baseline grid was constructed to capture near-wall viscous effects only. The momentum wake, shear flow, compression and expansion features were intentionally left under-resolved to simplify the manual gridding process.

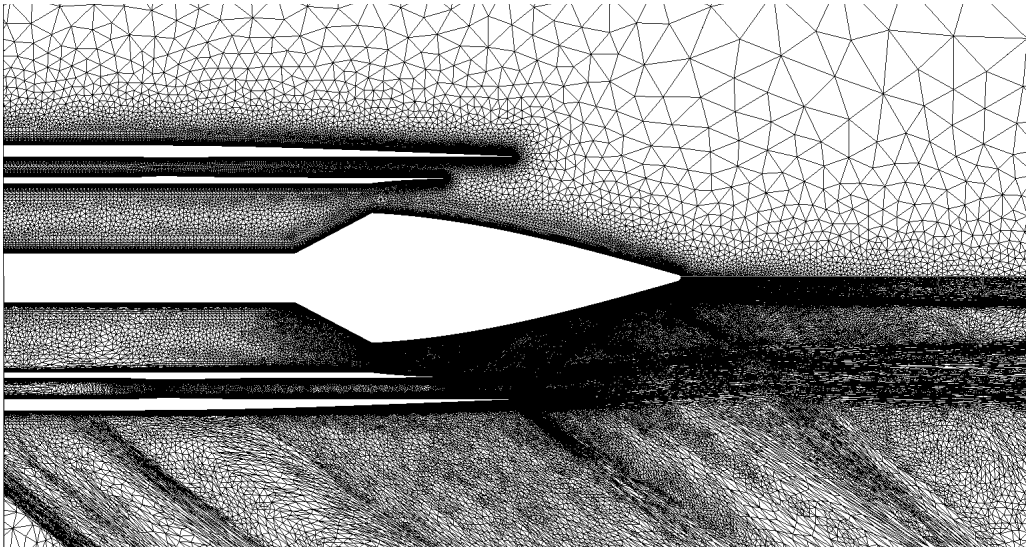


Fig 6. Top: Initial baseline body-fitted grid with anisotropic extruded cells near surface boundaries. Bottom: Output-adapted grid to reduce the discretization error of an off-body pressure integral taken one cowl diameter from the nozzle centerline.

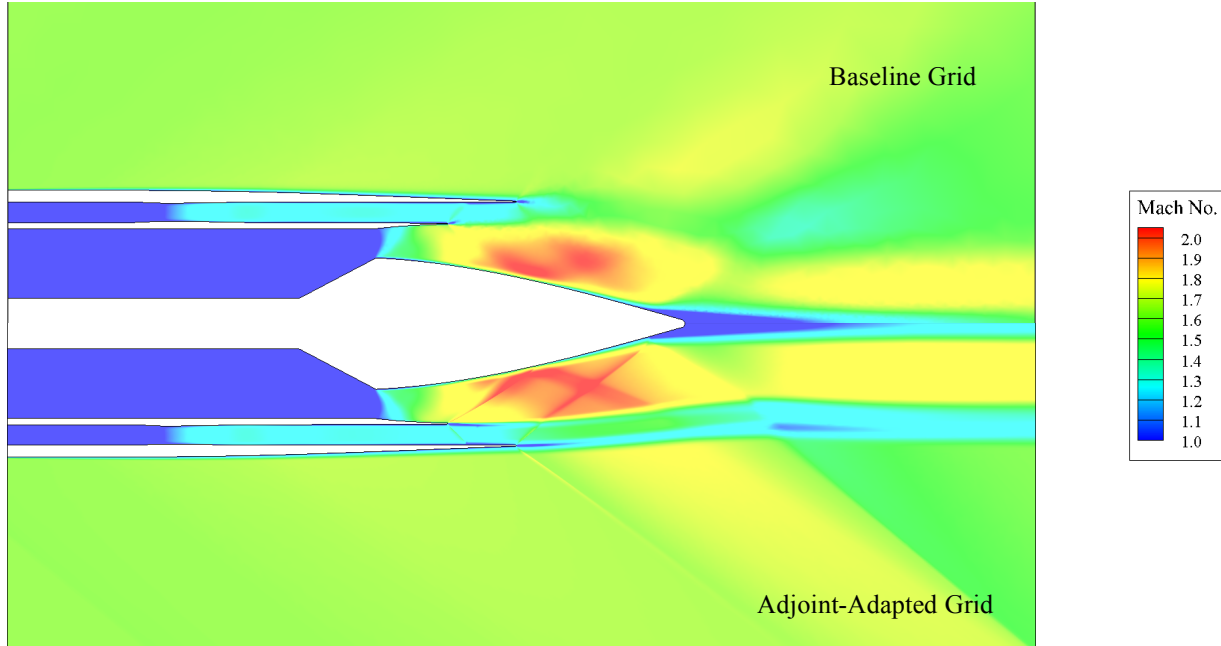


Fig. 7. Top: Mach number solution contour for non-adapted baseline grid. Bottom: Mach number solution contour for output-adapted grid.

Starting from the baseline discretization, output-based grid refinement²⁸ was performed to reduce the estimated discretization error of an off-body pressure integral taken one cowl diameter from the nozzle centerline. This focused the adaptation on refining the pressure deviation from freestream in the nearfield region. High aspect ratio elements near all body-fitted surfaces were frozen during the refinement process to avoid disruption of the viscous boundary layer discretization. Additional constraints were used to control maximum anisotropy and cell count during refinement steps. A total of 8 refinement iterations were performed to resolve details within the plume and increase cell density and quality in regions impacting the nearfield pressure signature. Grid refinement operations included node insertion, node movement, element collapse and element swap. The final adapted grid contained roughly 11.4 million nodes, approximately 3.25 times the number of nodes present in the baseline grid. The z-symmetry plane of the adapted grid along with a corresponding Mach number flow solution is shown in Figs. 7 and 8. While this grid was not adapted specifically to resolve thrust, the refinement increased cell densities in regions critical for thrust computation including the throat location of the core stream. The entire adjoint-based grid adaptation completed in approximately 24 hours of wall clock time utilizing 600 Intel Haswell processors.

VII. Adjoint-Based Design Optimization Results

Starting from the adapted baseline grid, the adjoint design capabilities of FUN3D were applied to reduce the nearfield pressure signature one cowl diameter from the nozzle centerline. The baseline and optimized geometries and Mach number solution contours are shown in Figs. 8 and 9. The scale of the axes has been adjusted in Fig. 8 to highlight geometric differences.

Comparison of the initial and final geometry profiles indicates the nozzle centerbody was lengthened and the curvature of the expansion side of the plug was reduced. The cowl was shortened and a subtle concavity was introduced on the outer cowl surface in contact with the freestream flow. The cowl centerline profile was adjusted near the exit, resulting in a higher trailing edge boattail angle for the optimized geometry. The length of the shroud was maintained and an increase in shroud trailing edge angle was also evident from optimization. Comparison of the baseline and optimized nozzle Mach number contours shows a subtle attenuation of compression features within the propulsive streamtube. The centerbody downstream extension resulted in diffused primary and reflected shocks within the core stream. The discrete flow expansion evident in the baseline solution near the cowl trailing edge is significantly diffused in the optimized solution. The bypass stream also appears to exit the bypass flowpath at a higher velocity in the optimized solution.

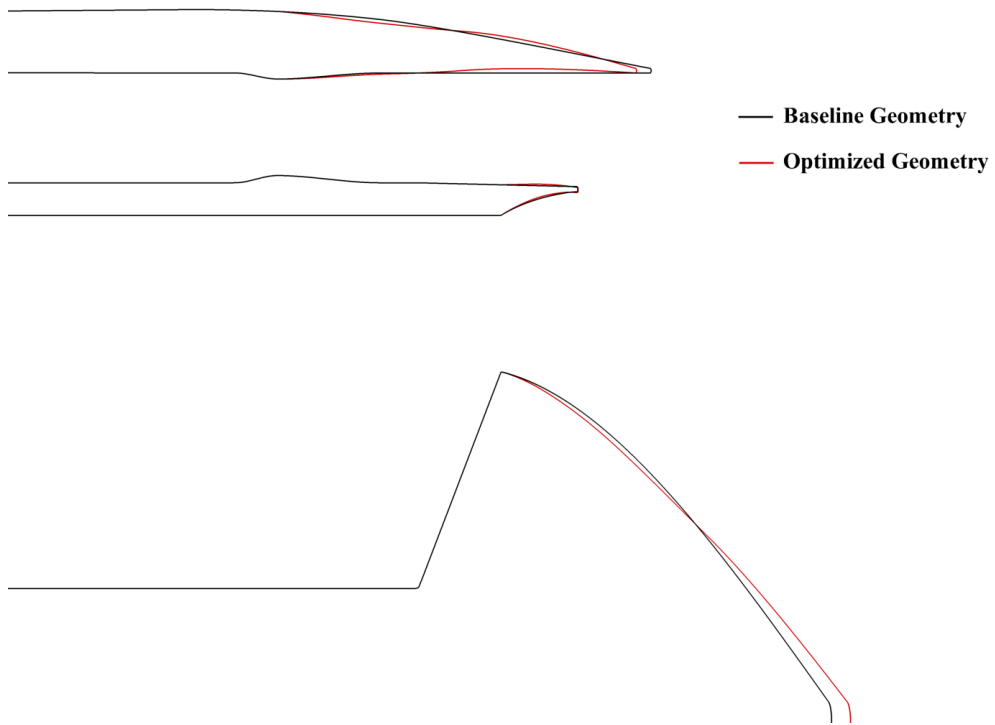


Fig 8. Comparison of baseline and optimized nozzle geometries for reducing nearfield pressure disturbances.

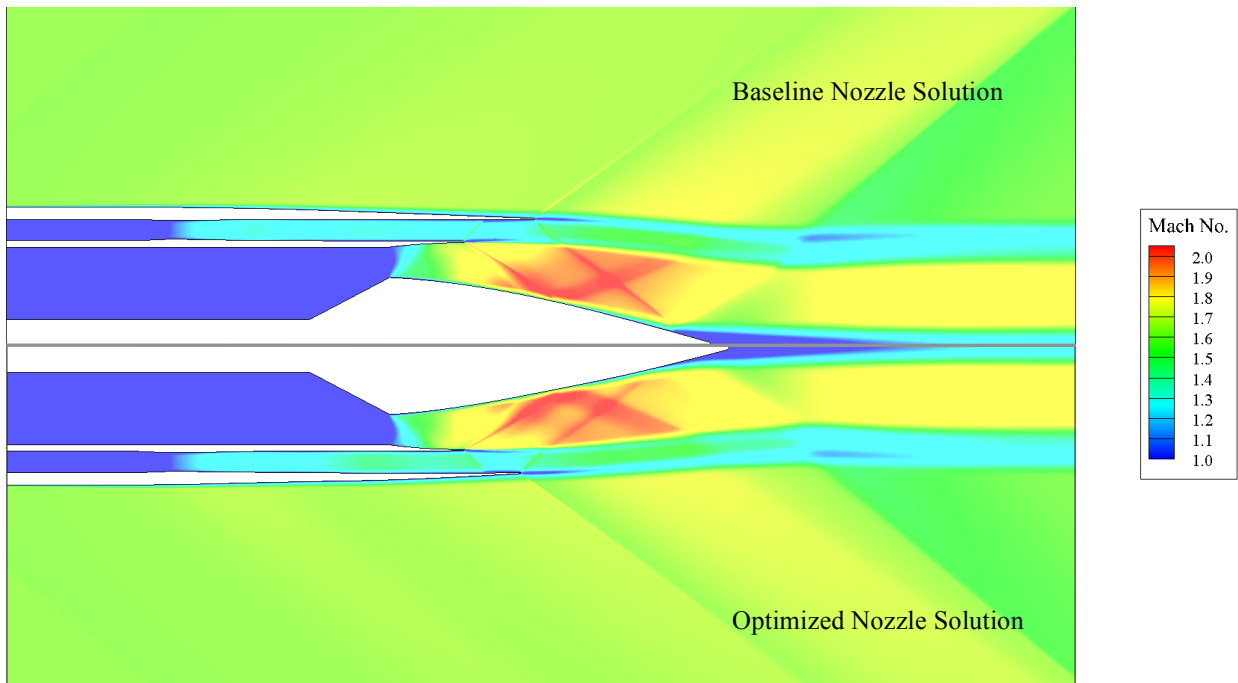


Fig. 9. Comparison of the baseline and optimized nozzle Mach number flow solutions for reducing nearfield pressure disturbances.

The baseline and optimized nearfield static pressure signatures taken with respect to the freestream reference pressure are plotted in Fig. 10. Note the optimized geometry exhibits a reduced under-pressure expansion near $x = 6.5$ -m. Variations to the external cowl introduced a pair of weak expansion/compression features evident between $x = 2.5$ -m and 5.0 -m. Given the bounds of the parameterization, it is likely these features were necessary to achieve the overall under-pressure reduction near $x = 6.5$ -m. The overpressure disturbance due to the nacelle trailing edge lip shock which occurs near $x = 7$ -m is also reduced when compared to the baseline signature. It is apparent the optimizer targeted the maximum and minimum peaks in the signature, which have the largest cost function impact.

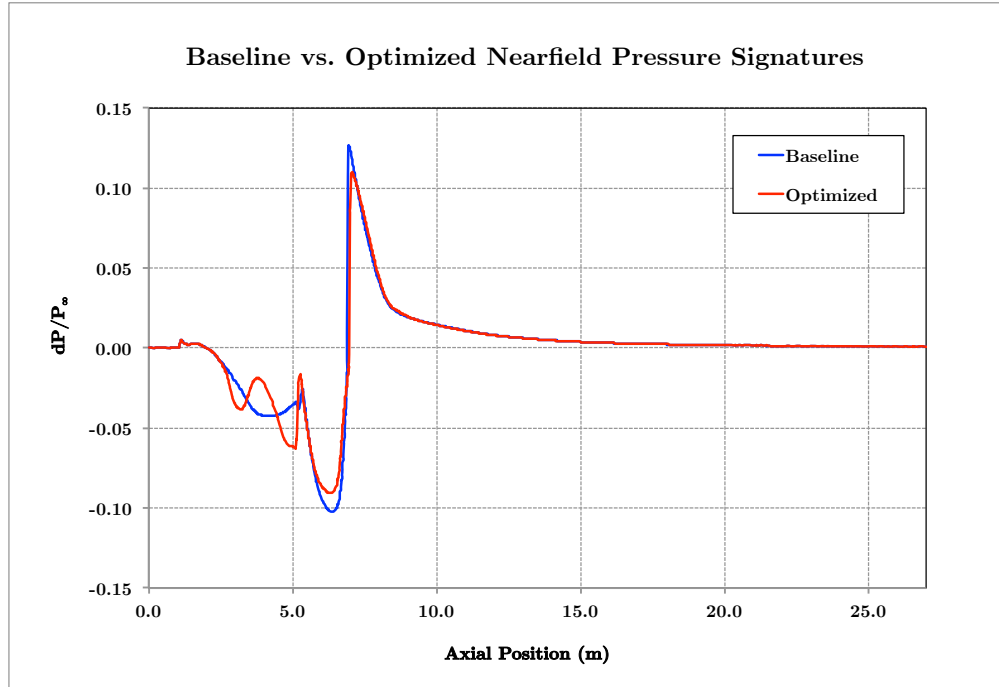


Fig. 10. Comparison of the baseline and optimized nozzle nearfield pressure signatures, extracted one cowl diameter from the nozzle centerline.

The thrust breakdown by component for the baseline and optimized geometries is listed in Table 2. Each value includes contributions of viscous forces, pressure forces and fluxes pertaining to each nozzle surface or inflow boundary, if applicable. As done for the geometry parameterization, the cowl and shroud were separated into inner and outer surfaces at the trailing edge. A 0.2% thrust increase is apparent for the optimized configuration. The majority of this thrust gain was due to variation in pressure forces acting on the nozzle centerbody. A small viscous drag increase for the plug due to axial extension was also observed, but not significant enough to offset the pressure force variation.

Component	Baseline Geometry	Optimized Geometry
Bypass Inflow	26478	26473
Core Inflow	96228	96238
Inner Cowl Surface	-1347	-1357
Outer Cowl Surface	-1525	-1552
Inner Shroud Surface	1505	1536
Outer Shroud Surface	-1158	-1190
Centerbody	-32121	-31914
Total	88059	88234

The optimization history is displayed in Fig. 11 and was terminated after 18 flow/adjoint cycles or 36 hours of wall clock time utilizing 600 Intel Haswell cores. The final nozzle design exhibited approximately a 12% reduction in the objective function relative to the baseline configuration. The optimizer converged predominately within just the first two iterations and approximately half of the control point bounds were found active upon termination.

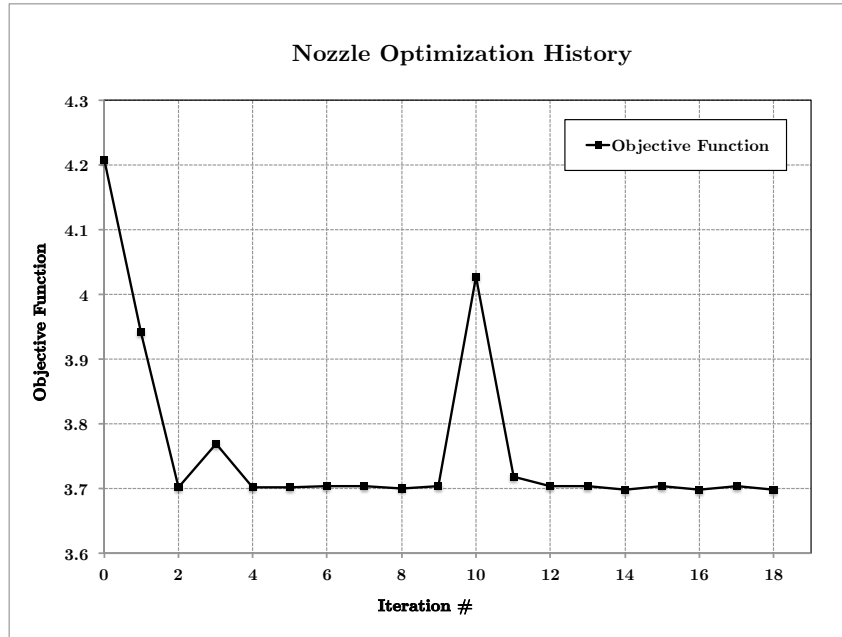


Fig 11. Nozzle optimization history.

VIII. Conclusion

Propulsion-airframe integration for ultra-low boom supersonic aircraft calls for improved methods to reduce off-body pressure disturbances introduced by the propulsion system or development of new methods for simultaneously tailoring propulsion system components in the presence of an airframe. This research aims at developing a method versatile enough to address both objectives.

This study marks a first-of-its-kind effort to apply gradient-based optimization coupled with the FUN3D adjoint design framework to mitigate nearfield compression/expansion features for an isolated dual-stream nozzle without compromising nozzle performance. Careful independent tailoring of the cowl, shroud and centerbody nozzle surfaces was found to enable subtle reduction to compression features in the propulsive streamtube while simultaneously permitting a 0.2% improvement in thrust at the design point condition. The objective function, which was posed as a summation of near-field pressure disturbances from freestream, was reduced by approximately 12%.

The optimization results imply that increasing the size of the design variable bounds would permit more geometric flexibility and further open the design space. Several challenges remain and must be addressed prior to performing more aggressive optimization studies. For example, permitting more substantial geometry variations were found to prove particularly challenging for the volume grid deformation mechanics, where negative volume elements were more likely to be produced. In addition, large shape changes alter the overall nozzle flow characteristics and deform the volume grid in a manner that numerically diffuses shock and expansion feature critical for nearfield signature prediction. Adjoint-based grid adaptation following each design iteration step would be the most desirable solution to overcome this limitation, but proves too computationally expensive at this time.

IX. Future Work

This research remains a work in progress and several follow-on activities are planned. Adjoint thrust derivatives will be implemented and validated within FUN3D. These will be used to replace the geometric bounds currently applied to avoid compromising core and bypass stream mass flow rates and enable geometric deformations to be introduced into the upstream core and bypass stream geometry. Improvements in robustness of the grid deformation process by solution of the linear elasticity equations will also be studied. The production of negative volume cells

during grid deformation frequently interrupted the design optimization process when large deformations were attempted. The high anisotropy of nearfield cells combined with sharp cowl/shroud trailing edges and symmetry plane constraints on allowable grid movement are probable causes. Alternate deformation functions may be considered or deformation from the baseline grid upon failure may be implemented as a work-around. The addition of an aggregate objective function that takes into account nozzle weight and uses volume as a potential surrogate is also of interest. The deformation methods developed here have been generalized and can be extended to reshape similar configurations, i.e. axisymmetric supersonic inlets. It is anticipated that extension to a B-spline surface-based parameterization will enable optimization of non-axisymmetric engine components and may also be investigated in future work.

X. Acknowledgements

The authors gratefully acknowledge the Commercial Supersonic Technology project of the Fundamental Aeronautics Program for supporting this work. The authors would also like to thank Nick Georgiadis for his assistance with validating the FUN3D thrust package along with Jon Seidel and Ray Castner for providing motivation for this research.

References

- ¹Aftomis, M. J., Nemec, M., Cliff, S. E., “Adjoint-Based Low-Boom Design with Cart3D,” In 29th AIAA Applied Aerodynamics Conference, AIAA Paper 2011-3500, Honolulu, HI, June 27–30, 2011.
- ²Li, W., Rallabhandi, S., “Inverse Design of Low-Boom Supersonic Concepts Using Reversed Equivalent-Area Targets,” In 29th AIAA Applied Aerodynamics Conference, AIAA Paper 2011-3498, Honolulu, HI, June 27-30, 2011.
- ³Rallabhandi, S. K., Nielsen, E. J., Diskin, B., “Sonic-Boom Mitigation through Aircraft Design and Adjoint Methodology,” In Journal of Aircraft, Vol. 51, No. 2, pp. 502-510, 2014.
- ⁴Palacios, F., Alonso, J. J., Colonno, M., Hicken, J., Lukaczyk, T., “Adjoint-based Method for Supersonic Aircraft Design using Equivalent Area Distributions,” In 50th AIAA Aerospace Sciences Meeting, AIAA Paper 2012-0269, Nashville, TN, January 9-12, 2012.
- ⁵Magee, T. E., Shaw, S. G., and Fugal, S. R., “Experimental Validations of a Low-Boom Aircraft Design,” 51st AIAA Aerospace Sciences Meeting, No. AIAA 2013-0646, AIAA, Grapevine, TX, January 7–10, 2013.
- ⁶Morgenstern, J. M., Buonanno, M., and Nordstrud, N., “N+2 Low Boom Wind Tunnel Model Design and Validation,” 30th AIAA Applied Aerodynamics Conference, No. AIAA 2012-3217, AIAA, New Orleans, LA, June 25–28, 2012.
- ⁷Wintzer, M., Castner, R., “Aircraft-Nozzle-Plume Interactions in the Context of Low Sonic Boom Design,” AIAA Science and Technology Exposition (SciTech), Manuscript Submitted for Publication, Kissimmee, FL, January 5-9, 2015.
- ⁸Wintzer, M., Kroo, I. M., Aftomis, M. J., and Nemec, M., “Conceptual Design of Low Sonic Boom Aircraft Using Adjoint-Based CFD,” Seventh International Conference on Computational Fluid Dynamics, Paper No. ICCFD7-2005, ICCFD, Big Island, HI, July 2012.
- ⁹Castner, R., Zaman, K., Fagan, A., Heath, C., “Wedge Shock and Nozzle Exhaust Plume Interaction in a Supersonic Jet Flow,” In 52nd Aerospace Sciences Meeting, AIAA Paper 2014-0232, National Harbor, MD, January 13-17, 2014.
- ¹⁰Conners, T. R., Henne, P.A., Howe, D. C. “A Method for Reducing Sonic Boom Strength by Tailoring the Shape of the Propulsive Streamtube,” In 49th AIAA/ASME/SAE/ASEE Joint Propulsion Conference, AIAA Paper 2013-3678, San Jose, CA, July 14-17, 2013.
- ¹¹Biedron, R. T., Derlaga, J. M., Gnoffo, P. A., Hammond, D. P., Jones, W. T., Kleb, B., Lee-Rausch, E. M., Nielsen, E. J., Park, M. A., Rumsey, C.L., Thomas, J. L., Wood, W. A., “FUN3D Manual: 12.4,” NASA TM-2014-218179, 2014.
- ¹²Conners, T. R., and Wayman, T. R., “The Feasibility of High-Flow Nacelle Bypass for Low Sonic Boom Propulsion System Design,” In 29th AIAA Applied Aerodynamics Conference, AIAA Paper 2011-3797, Honolulu, HI, June 27-30, 2011.
- ¹³Conners, T. R., Gulfstream Aerospace Corporation, Savannah, GA, U.S. Patent Application for “Low Shock Strength Propulsion System,” Publications No. US 2010/0043389, Feb. 25, 2010, and No. US 2013/0062424 A1, Mar. 14, 2013.

- ¹⁴Georgiadis, N. J., Yoder, D. A., Towne, C. E., Engblom, W. A., Bhagwandin, V., Power, G. D., Lankford, D. W., and Nelson, C. C., “Wind-US Physical Modeling Improvements to Complement Hypersonic Testing and Evaluation,” In 47th AIAA Aerospace Sciences Meeting, AIAA Paper 2009-193, Orlando, FL, January 5-8, 2009.
- ¹⁵Nelson, C., “An Overview of the NPARC Alliance’s Wind-US Flow Solver,” In 48th AIAA Aerospace Science Meeting, AIAA Paper 2010-27, January 4-7, 2010.
- ¹⁶de Boor, C., “A Practical Guide to Splines (Revised Ed.)”, In Applied Mathematical Sciences, Vol. 27, Springer, Berlin, 2011.
- ¹⁷Roe, P. L., “Approximate Riemann Solvers, Parameter Vectors, and Difference Schemes,” In Journal of Computational Physics, Vol. 43, Issue 2, pp. 357–72, October 1981.
- ¹⁸Spalart, P. R. and Allmaras, S. R., “A One-Equation Turbulence Model for Aerodynamic Flows,” La Recherche Aeronautique, No. 1, pp. 5-21, 1994.
- ¹⁹Nielsen, E. J. and Anderson, W. K., “Recent Improvements in Aerodynamic Design Optimization on Unstructured Meshes,” In AIAA Journal, Vol. 40, No. 6, pp. 1155-1163, 2002. See also AIAA Paper 2001-596.
- ²⁰Nielsen, E. J., “Aerodynamic Design Sensitivities on an Unstructured Mesh Using the Navier-Stokes Equations and a Discrete Adjoint Formulation,” Ph.D. Thesis, Virginia Polytechnic Institute and State University, 1998.
- ²¹Nielsen, E. J., and Diskin B., “Discrete Adjoint-Based Design for Unsteady Turbulent Flows on Dynamic Overset Unstructured Grids,” AIAA Journal, Vol. 51, No. 6, pp. 1355-1373, June 2013.
- ²²Giles, M., Duta, M., Müller, J.-D., and Pierce, N., “Algorithm Developments for Discrete Adjoint Methods,” AIAA Journal, Vol. 41, No. 2, 2003, pp. 198-205, See also AIAA Paper 2001-2596.
- ²³Nielsen, E. J., Lu, J., Park, M. A., and Darmofal, D. L., “An Implicit, Exact Dual Adjoint Solution Method for Turbulent Flows on Unstructured Grids,” In Computers and Fluids, Vol. 33, No. 9, 2004, pp. 1131-1155, See also AIAA Paper 2003-272.
- ²⁴Biedron, R. T., and Thomas, J. L., “Recent Enhancements To The FUN3D Flow Solver For Moving-Mesh Applications,” AIAA-2009-1360, January 2009.
- ²⁵Saad, Y. and Schultz, M. H., “GMRES: A Generalized Minimum Residual Algorithm for Solving Nonsymmetric Linear Systems,” SIAM Journal of Scientific and Statistical Computing, Vol. 7, 1986, pp. 856–869.
- ²⁶Lyu, Z., and Martins, J. R. R. A., “Aerodynamic Design Optimization Studies of a Blended-Wing-Body Aircraft”, In Journal of Aircraft, Vol. 51, No. 5, pp. 1604-1617, 2014.
- ²⁷Gill, P. E., Murray, W., and Saunders, M. A., “User’s Guide for SNOPT Version 7: Software for Large-Scale Nonlinear Programming,” June, 2008.
- ²⁸Park, M. A., Carlson, J., “Turbulent Output-Based Anisotropic Adaptation,” In 48th AIAA AeroSciences Meeting, AIAA Paper 2010-0168, Orlando, FL, January 4-7.